TU Delft

Delft University of Technology

# Analysis of shielding of propeller noise using beamforming and predictions

Vieira, Ana; Snellen, Mirjam; Malgoezar, Anwar M.N.; Merino-Martinez, Roberto; Simons, Dick G.

**DOI**
10.1121/1.5121398

**Publication date**
2019

**Document Version**
Final published version

**Published in**
Journal of the Acoustical Society of America

**Citation (APA)**
Vieira, A., Snellen, M., Malgoezar, A. M. N., Merino-Martinez, R., & Simons, D. G. (2019). Analysis of shielding of propeller noise using beamforming and predictions. *Journal of the Acoustical Society of America*, *146*(2), 1085-1098. https://doi.org/10.1121/1.5121398

**Important note**
To cite this publication, please use the final published version (if applicable).
Please check the document version above.

**Copyright**
Other than for strictly personal use, it is not permitted to download, forward or distribute the text or part of it, without the consent of the author(s) and/or copyright holder(s), unless the work is under an open content license such as Creative Commons.

**Takedown policy**
Please contact us and provide details if you believe this document breaches copyrights.
We will remove access to the work immediately and investigate your claim.

*This work is downloaded from Delft University of Technology.*
*For technical reasons the number of authors shown on this cover page is limited to a maximum of 10.*

# Analysis of shielding of propeller noise using beamforming and predictions

Ana Vieira, Mirjam Snellen, Anwar M. N. Malgoezar, Roberto Merino-Martinez, and Dick G. Simons

Citation: The Journal of the Acoustical Society of America **146**, 1085 (2019); doi: 10.1121/1.5121398
View online: https://doi.org/10.1121/1.5121398
View Table of Contents: https://asa.scitation.org/toc/jas/146/2
Published by the Acoustical Society of America

**ARTICLES YOU MAY BE INTERESTED IN**

Scattering and radiation force dependence on properties of empty elastic spherical shells: Low-frequency phase-shift derivation
The Journal of the Acoustical Society of America **146**, EL145 (2019); https://doi.org/10.1121/1.5121576

The edge bending wave on a plate reinforced by a beam (L)
The Journal of the Acoustical Society of America **146**, 1061 (2019); https://doi.org/10.1121/1.5121315

Broadband acoustic signal variability induced by internal solitary waves and semidiurnal internal tides in the northeastern East China Sea
The Journal of the Acoustical Society of America **146**, 1110 (2019); https://doi.org/10.1121/1.5121715

Hybrid Cramér-Rao bound of direction finding, using a triad of cardioid sensors that are perpendicularly oriented and spatially collocated
The Journal of the Acoustical Society of America **146**, 1099 (2019); https://doi.org/10.1121/1.5120521

Cognitive load elevates discrimination thresholds of duration, intensity, and $f_0$ for a synthesized vowel
The Journal of the Acoustical Society of America **146**, 1077 (2019); https://doi.org/10.1121/1.5120404

The effect of target/masker fundamental frequency contour similarity on masked-speech recognition
The Journal of the Acoustical Society of America **146**, 1065 (2019); https://doi.org/10.1121/1.5121314

# Analysis of shielding of propeller noise using beamforming and predictions

Ana Vieira,[a] Mirjam Snellen, Anwar M. N. Malgoezar, Roberto Merino-Martinez, and Dick G. Simons

*Section Aircraft Noise and Climate Effects, Faculty of Aerospace Engineering, Delft University of Technology, 2629 HS Delft, The Netherlands*

(Received 15 April 2019; revised 22 July 2019; accepted 24 July 2019; published online 12 August 2019)

Engine noise shielding is an important measure towards low-noise aircraft configurations. Such designs are supported by prediction tools that indicate high values for shielding of engine noise. Most prediction models approximate the complex nature of engine noise to simple noise sources such as monopoles or dipoles. This work compares predictions of noise shielding with experiments using different noise sources and shielding body geometries. The experiments considered in this work concern a monopole source shielded by a flat plate and a NACA 64-008 A wing, and a propeller shielded by the same wing. Comparisons between models and measurements are made by analysis of noise levels at individual microphones and using conventional beamforming. Results show that for the monopole cases the model predictions are in agreement with the experimental data, with an average deviation of 2–3 dB. The curvature of the leading edge of the wing influences the noise shielding results. The measured values of noise shielding of propeller noise are lower than those measured for the omni-directional source. Different types of source directivity are used to approximate the propeller in the predictions: monopole, dipole and a multi-source. The dipole approximation shows the best agreement with the experiments for the case of the propeller.
© *2019 Acoustical Society of America*. https://doi.org/10.1121/1.5121398

[AGP] Pages: 1085–1098

## I. INTRODUCTION

The continuous expansion of air traffic raises concerns about the high levels of perceived noise around airports due to its negative effects on human health (Lu and Morrell, 2006). Recent concepts for the next generation of aircraft reflect a growing awareness that current noise reduction technologies are insufficient to significantly decrease noise levels on the ground. Low-noise concepts, such as the blended-wing body (BWB) (Guo *et al.*, 2015) and airframe distributed propulsion (Synodinos *et al.*, 2017), are highly dependent on engine noise shielding by the airframe structure.

The high values of noise shielding predictions in early research motivated such new aircraft designs and encouraged further work in this field. Most modeling approaches to the problem of noise shielding consider the shielding body as a rigid sharp surface and the source as a monopole. Such approximations are considered reasonable for an initial estimate of engine noise shielding in the design of a new aircraft concept. The large dimensions of the aircraft and distances between sources and observers together with the complex nature of the engine noise emissions result in computational times of computer fluid dynamics simulations incompatible with an optimization procedure required in the design phase of an aircraft (Manoha *et al.*, 2010).

More recent research on this topic questions the validity of approximating a complex source as an engine with a monopole source (Turkdogru *et al.*, 2013), even for rough estimates. Also, a first comparison between noise shielding predictions and experimental data from aircraft flyovers under operational conditions (Vieira *et al.*, 2018) indicates that predictions overestimate noise shielding by a few decibels.

In order to further understand noise shielding, this work compares experimental data with predictions for different cases that are considered to be representative for noise shielding at an aircraft. The model used in the predictions is based on the Kirchhoff integral theory and the modified theory of physical optics (MTPO) (Colas and Spakovszky, 2013; Umul, 2004). The method is based on first principles with approximations in the boundary conditions. It is therefore more accurate than semi-empirical methods such as the Barrier Shielding Method (Maekawa, 1968). On the other hand, high accuracy methods such as the boundary element method (Kirkup, 2007), the equivalent source method (Dunn and Tinetti, 2004) and the ray-tracing method (Agarwal *et al.*, 2007) require high performance computing in order to be implemented in a multidisciplinary design optimization of an aircraft. The MTPO based method used in this work is considered as accurate and time-efficient and therefore suitable to be applied in the design cycle of an aircraft.

The comparison between predictions and experimental data is made by comparing the sound pressure levels over a microphone array and also by using beamforming to image the source distribution over the shielding surface.

The first case analyzed is a rectangular flat plate with an omni-directional source emitting white noise. The relative distances between the source, the plate and the array are

[a]Electronic mail: A.E.AlvesVieira@tudelft.nl

varied. The values of noise shielding are assessed for different frequencies.

The plate is then replaced by a NACA wing (64-008 A) in order to assess the agreement between predictions and experimental data when the shielding object has a smooth edge with curvature (leading edge) that can induce creeping rays. Finally, the omni-directional source is replaced by a small propeller, which is a representative case of noise shielding for novel aircraft configurations. Significant differences between predictions and experimental data are expected in this case (Turkdogru *et al.*, 2013) due to the complex nature of the source. Therefore, different source directivity patterns are implemented in the prediction model in addition to the monopole: a dipole and a multi-source (a ring of monopoles). The parameters varied for the simulations with the multi-source were the total number of monopole sources, their radial location in the propeller disk, and the azimuthal rotating modes.

This work aims to understand to what extent noise shielding is affected by the shielding body geometry (influence of smooth edges) and, more importantly, by the directivity of the noise source, which is often neglected or roughly approximated in predictions. Beamforming (using both experimental data and predictions) is an important tool to better understand the behavior of noise shielding. Therefore, the analyses are not limited to a quantitative description (absolute values of noise shielding) and spatial description (values obtained at different observer points) of noise shielding, but also include a visual characterization (source distribution on the edges of the shielding body) using beamforming.

In this paper, Section II is a summary of the theoretical work on noise shielding and beamforming applied in this work. Section III describes the experimental setup and the acoustic array optimized for beamforming. The comparison between experimental data and predictions is presented in Sec. IV and the main conclusions are summarized in Sec. V.

## II. METHODS

### A. Noise shielding prediction method

The shielding of engine noise by the aircraft structure is a complex problem, which results in large computational times. For that reason, it is important to use a method that has a good trade-off between accuracy of the results and computational time. In this work a method based on the Kirchhoff integral theory built on MTPO is considered a suitable approach to predict engine noise shielding. This section provides a brief summary of this method. For more details the reader is referred to Colas and Spakovszky (2013), Umul (2004), and Vieira *et al.* (2018).

Consider an arbitrary aperture $\sigma$ in a screen $\bar{\sigma}$, shown in Fig. 1, between a source at position $\mathbf{x}_s$ and a receiver at position $\mathbf{x}$.

The scattered pressure field $p_s$ and the pressure field emitted by the source $p_i$ follow the Helmholtz equation in a volume of control that excludes the screen surface $\bar{\sigma}$ and the source location. An expression of the scattered pressure field in the aperture is obtained following the procedure:

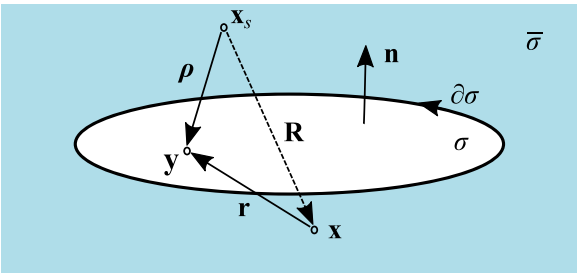


FIG. 1. (Color online) Kirchhoff integration across the circular aperture $\sigma$ in the screen $\bar{\sigma}$.

- apply the Gauss and Green theorems in the volume of control mentioned above,
- consider that the scattered pressure field is zero on the screen,
- consider that the scattered pressure field approximates to zero far from the screen,
- assume that the scattered field is equal to the emitted field in the aperture $\sigma$.

These steps result in Eq. (1) for the scattering pressure field at $\mathbf{x}$,

$$p_s^{\text{aperture}} = \frac{1}{4\pi}\int_\sigma \left[ p_i \mathbf{n}\cdot\nabla\frac{e^{ik|\mathbf{r}|}}{|\mathbf{r}|} - \frac{e^{ik|\mathbf{r}|}}{|\mathbf{r}|}\mathbf{n}\cdot\nabla p_i \right] dS, \tag{1}$$

where $\mathbf{r} = \mathbf{y} - \mathbf{x}$, $\mathbf{y}$ is located at the aperture, and $k = 2\pi f/c$ is the wavenumber, in which $c$ is the speed of sound.

Evaluation of the surface integral in Eq. (1) is computationally demanding, so it is simplified using the theory of the diffracted waves. This theory states that the scattered pressure field is given by the undisturbed incident pressure field $p_{GO}$ and the boundary diffracted field $p_d$,

$$p_s^{\text{aperture}} = p_{GO} + p_d. \tag{2}$$

Here, $p_{GO} = p_i\chi$, where $\chi$ is a delta function equal to unity when the ray from source to receiver passes through the aperture $\sigma$ and zero otherwise.

Maggi and Rubinowicz (Miyamoto and Wolf, 1962) derived an expression for the diffracted field written in terms of a line integral $\partial\sigma$, which results in a significant decrease of computational time,

$$p_d = \frac{1}{4\pi}\oint_{\partial\sigma} \frac{e^{ik|\boldsymbol{\rho}|}}{|\boldsymbol{\rho}|}\frac{e^{ik|\mathbf{r}|}}{|\mathbf{r}|}\frac{(\boldsymbol{\rho}\times\mathbf{r})\cdot d\mathbf{s}}{|\boldsymbol{\rho}||\mathbf{r}| + \boldsymbol{\rho}\cdot\mathbf{r}}, \tag{3}$$

where $\boldsymbol{\rho} = \mathbf{y} - \mathbf{x}_s$ (see Fig. 1).

Extending this work, Miyamoto and Wolf (1962) included the expression to not be limited to spherical nor plane waves for the incident field. Using an asymptotic expansion they derived

$$p_d = \frac{1}{4\pi}\oint_{\partial\sigma} p_i(|\boldsymbol{\rho}|)\frac{e^{ik|\mathbf{r}|}}{|\mathbf{r}|}\frac{(\boldsymbol{\rho}\times\mathbf{r})\cdot d\mathbf{s}}{|\boldsymbol{\rho}||\mathbf{r}| + \boldsymbol{\rho}\cdot\mathbf{r}}, \tag{4}$$

which allows for the inclusion of the directivity of the noise source.

The line integral of Eq. (4) can be discretized in straight line segments $\Gamma$, and the diffraction field can be expressed as

$$I_\Gamma = \frac{1}{4\pi}\int_\Gamma \frac{1}{|\boldsymbol{\rho}|}\frac{1}{|\mathbf{r}|}\frac{(\boldsymbol{\rho}\times\mathbf{r})\cdot d\mathbf{s}}{|\boldsymbol{\rho}||\mathbf{r}|+\boldsymbol{\rho}\cdot\mathbf{r}} e^{ik(|\boldsymbol{\rho}|+|\mathbf{r}|)}. \tag{5}$$

Equation (5) can rewritten as

$$I_\Gamma = \int_\Gamma f(s)e^{ikg(s)}ds, \tag{6}$$

where $f(s)$ is the amplitude of the function to be integrated and $g(s)$ is the phase. The integral is solved using the method of the stationary phase and the uniform theory of diffraction to avoid singularities (Lewist and Boersma, 1969; Sommerfeld, 2004).

For the case of a smooth edge with a curvature, as represented in Fig. 2, the amplitude $f(s)$ is modified by assuming that the diffracted field $p_d$ is equal to the diffracted field defined by the geometrical theory of diffraction (Leppington, 1970; Pathak *et al.*, 1979) for edges with a curvature,

$$p_d^{\mathrm{GTD}} = p_i e^{ik|\mathbf{r}|}\sqrt{\frac{|\mathbf{r_p}|}{|\mathbf{r_p}|(|\mathbf{r}|+|\mathbf{r_p}|)}}\sum_m D_m^2(k,a)e^{-t\alpha_m}e^{ikt}. \tag{7}$$

Here, $t$ is the arc length between two points $P_1$ and $P_2$. These two points correspond to the grazing incidence of sound to the curve from the source and receiver, respectively. The variable $\mathbf{r_p}$ is the distance between $P_1$ and $P_2$ and $a$ is the local radius of the object. $D_m$ and $\alpha_m$ are the diffraction and decay coefficients, given by

$$D_m^2(k,a) = \frac{e^{i\pi/12}a^{1/2}}{2^{5/6}\pi^{1/2}(ka)^{1/6}Ai(-q_m)^2}, \tag{8}$$

$$\alpha_m = \frac{1}{a}\left(\frac{ka}{2}\right)^{1/3} q_m e^{-i(\pi/6)}. \tag{9}$$

In Eq. (8) $Ai$ is the Airy function and $q_m$ is the $m$th root of its first derivative.

The resultant expression of $f(s)$ for a smooth edge is then

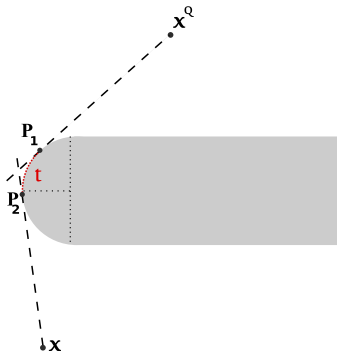


FIG. 2. (Color online) Representation of a smooth edge and the tangent points from the noise source are receiver.

$$f(s) = e^{-\pi/4}\sqrt{\frac{k}{2\pi}}\sqrt{\frac{|\mathbf{d}|}{|\mathbf{r}|(|\mathbf{d}|+|\mathbf{r}|)}}\sqrt{\frac{|\boldsymbol{\rho}|+|\mathbf{r}|}{|\boldsymbol{\rho}|\mathbf{r}||}}\sum_m D_m^2 e^{-t\alpha_m}e^{ikt}. \tag{10}$$

Finally, in order to calculate the scattered field due to the presence of the shielding object, $p_s^{\mathrm{object}}$, the obstacle is interchanged with the aperture in the screen, following Babinet's principle (Born and Wolf, 1999),

$$p_s^{\mathrm{object}} = p_i - p_s^{\mathrm{aperture}}. \tag{11}$$

In this work three types of incident fields are considered: a monopole source, a dipole, and a multi-source composed by a ring of monopoles. The monopole expression is given by

$$p_{i,\mathrm{monopole}} = \frac{e^{ik|\boldsymbol{R}|}}{|\boldsymbol{R}|} \tag{12}$$

and the dipole by

$$p_{i,\mathrm{dipole}} = \frac{k^2}{|\boldsymbol{R}|}d\cos(\theta)e^{-ik|\boldsymbol{R}|}, \tag{13}$$

where $\theta$ is the polar angle and $d$ the distance for which $kd \ll 1$.

Non compact sources such as propellers and fans generate harmonic rotating modes, and in this work $N$ monopoles were distributed along a circle at half span of the blade to simulate such behavior. Each monopole $j$ is characterized by an amplitude $A_0$, frequency $f$ and phase $\phi_j$,

$$p_j = A_0\frac{e^{ik\mathbf{R}+in\phi_j-i\omega t}}{\mathbf{R}}. \tag{14}$$

Here, $p_j$ is the acoustic pressure of the monopole $j$ and $n$ is the azimuthal number that generates the azimuthal rotating modes. In this case all the monopoles have the same amplitude $A_0$. The noise shielding is averaged over time, so the time dependence of $p_j$ is not considered.

The method for prediction of noise shielding described above is valid if the following conditions are verified:

(1) $\lambda \le l$ and $\lambda \ll r$, in which $l$ is the length of the edges of the shielding object,
(2) $kd_{\mathrm{obs}} \ge 1$, with $d_{\mathrm{obs}}$ the distance between source and observers, so the observers are in the far-field,
(3) $ka > 1$, for an edge with curvature.

In this work, noise shielding is defined as the difference between the scattered field by the object and the incident field,

$$\Delta L_p = 20\log_{10}\left|\frac{p_s^{\mathrm{object}}}{p_i}\right|, \tag{15}$$

where $\Delta L_p$ is the so-called shielding factor, in dB. A negative value of $\Delta L_p$ indicates a decrease in the noise level, i.e., noise shielding.

### B. Beamforming

Using a set of microphones simultaneously and recording the signals not only makes it possible to analyse the

sound pressure levels over different angles, but also to use them collectively to both localize and quantify sound sources. This is known as beamforming. Beamforming is a widely applied signal processing technique to spatially filter the signals to either directionally receive or transmit a signal.

In the current work a set of 64 microphones was used to receive the signals. This allows one to determine where sound sources were present together with their levels. In order to perform beamforming, use is made of the pressure time signal at each microphone. The set of microphone signals is given as the vector $\mathbf{p}(t) \in \mathbb{R}^{N\times 1}$, where $N$ is the number of microphones. After transforming the signal to the frequency domain $\mathbf{p}(\omega)$, we can construct the so-called cross spectral matrix (CSM) as

$$\mathbf{C}(\omega) = \mathbb{E}[\mathbf{p}(\omega)\mathbf{p}^*(\omega)], \tag{16}$$

where $\mathbb{E}(\cdot)$ is the expectation operator and $(\cdot)^*$ the complex conjugate transpose. In practice this means that the time signal is divided into many blocks and the CSM calculated as an average.

The source power estimate, and thus the resultant beamformer output, for a given scan point $\mathbf{x}_t$ is then given as

$$B(\mathbf{x}_t, \omega) = \mathbf{h}^*(\mathbf{x}_t)\mathbf{C}\mathbf{h}(\mathbf{x}_t), \tag{17}$$

where $\mathbf{h}(\mathbf{x}_t) \in \mathbb{C}^{N\times 1}$ is the steering vector and contains the microphone array responses of potential sources. For the steering vector we use formulation III of (Sarradj, 2012). For the $n$th element this is given by

$$h_n = \frac{1}{r_{t,n}r_{t,0}\sum_{n=1}^{N}\left(1/r_{t,n}^2\right)} e^{-j\omega(r_{t,n}-r_{t,0})/c}, \tag{18}$$

where $r_{t,n} = |\mathbf{x}_t - \mathbf{x}_n|$ is the distance between the scan point and microphone $n$, $r_{t,0} = |\mathbf{x}_t - \mathbf{x}_0|$ the distance between the scan point and the center of the array, and $c$ the speed of sound. A schematic can be seen in Fig. 3.

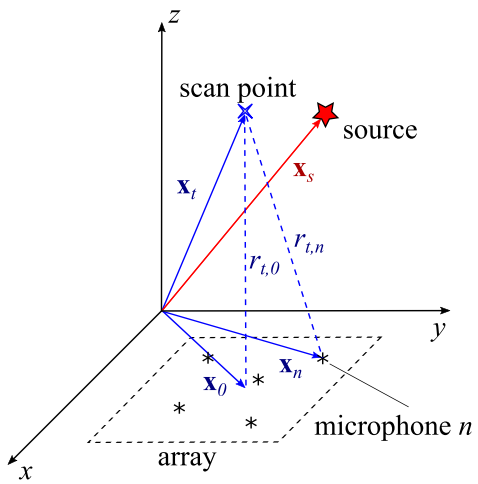


FIG. 3. (Color online) Microphone array and distances to the scan point, where $\mathbf{x}_0$ is the center of the array, $\mathbf{x}_n$ the position of microphone $n$, $\mathbf{x}_t$ the position of the scan point, and $\mathbf{x}_s$ the position of the source. In this example the scan point does not match the source position, i.e., $\mathbf{x}_t \neq \mathbf{x}_s$.

Equation (17) is known as conventional beamforming. The general approach is to define a number of scan points and estimate the source powers for each point using Eq. (17). The sound pressure level value at the array centre $\mathbf{x}_0$ can then be found as

$$L_p(\mathbf{x}_t, \omega) = 20\log_{10}\left(\frac{\sqrt{B(\mathbf{x}_t, \omega)}}{p_0}\right), \tag{19}$$

with $p_0 = 20$ $\mu$Pa, the reference pressure.

The levels are often depicted as a source map and the grid points usually lie in a plane. For the resultant image, high levels indicate the presence of a source $\mathbf{x}_t = \mathbf{x}_s$, whereas low levels indicate a mismatch, $\mathbf{x}_t \neq \mathbf{x}_s$.

In this work beamforming is performed using both predictions and experimental data. To have a fair comparison the predictions will be sampled in space at the same positions where the microphones are situated.

## III. EXPERIMENTAL SETUP

### A. The anechoic room and acoustic array

The sound pressures were measured using a microphone array in an anechoic room. The array consists of 64 G.R.A.S. 40PH CCP free-field array microphones (G.R.A.S. 40 PH CCP, "G.R.A.S. Sound and Vibration 40 PH CCP Free field array microphone"). The microphones were calibrated individually using a G.R.A.S. 42AA pistonphone (G.R.A.S. Pistonphone, "G.R.A.S. Sound and Vibration 42AA Pistonphone class 1"). The microphones are positioned in a metal grid using the TU Delft Optimized Array distribution (Luesutthiviboon *et al.*, 2018; Malgoezar *et al.*, 2016). This configuration is used as it provides the best trade-off for the main lobe width and maximum sidelobe level in beamforming. The structure of the microphone array is shown in Fig. 4 and a clear distribution of the microphones can be seen in Fig. 8.

The microphones are connected to a National Instruments data acquisition (DAQ) system. The system consists of a NI PXIe-1085 rack and has five PXIe-4499 Sound and vibration

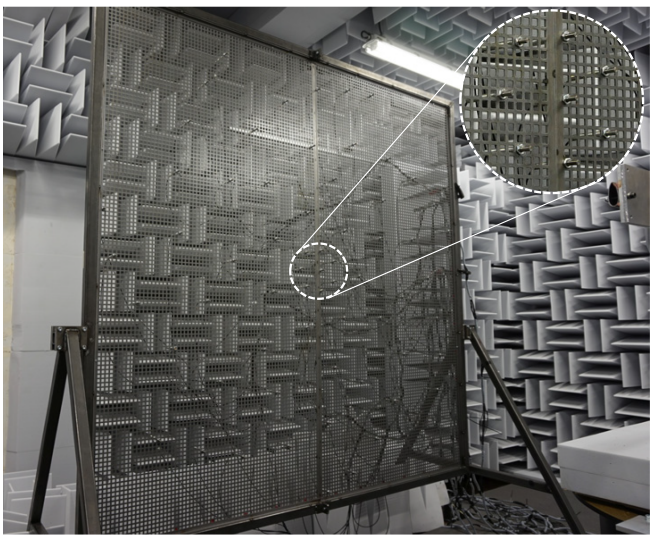

FIG. 4. (Color online) The TU Delft Optimized microphone array.

data acquisition modules. Each microphone is connected using a RG174AU 50 Ω impedance cable, equaling 10 m in length. Eight microphones are bundled together and connected to a NI SHB4X-8BNC Infiniband to BNC conversion cable, allowing them to be connected to the DAQ-system.

The array was designed to reduce acoustic reflections (Vlemmix, 2017) and the free-field behaviour of the anechoic room was assessed following the ISO 3745 guidelines (ISO, 2012a). The average reverberation time is 0.25 s, corresponding to the anechoic category of ISO 3382 (ISO, 2012b).

The vertical wind tunnel is placed in the center of the anechoic room and has a circular shape with a 60 cm diameter. In the experiments with incoming airflow the flow speed was set constant at 10 m/s.

In this work a sampling frequency of 50 kHz is used. The recording time for every microphone is set to 60 s. After acquiring the signal the sound pressure level values can be calculated directly.

Throughout this work, noise shielding is calculated considering certain frequency bands of interest. For band-passing the signal a fourth order digital Butterworth filter is applied. Butterworth filters are designed to have the magnitude for the frequency response to be as flat as possible in the pass-band (Oppenheim *et al.*, 1997), which is desirable to obtain correct levels of the sound pressure level in the given band. A fourth order filter is selected as it provides a good trade off for the roll off in the stopband (−24 dB per octave) and good stability in the frequency domain.

For beamforming, the CSM is constructed for the desired frequency band from Eq. (16) using time blocks of 1 s and an overlap of 50%. This results in a frequency resolution of $\Delta f = 1$ Hz.

### B. Sound sources

An omni-directional sound source is used for the first experiments presented in Sec. IV A. The source is a customized miniature sound source type QINDW developed by QSOURCES. It has an oblong shape with a length of 11 cm and a diameter of 2 cm (see Fig. 5). The source sound power is omnidirectional in the azimuthal plane and has a flat frequency response from approximately 500 Hz to 6.3 kHz when driven by white noise.

A small propeller is used as the sound source in the second set of experiments in Sec. IV B. The propeller is a three-blade Master Airscrew E-MA1260T with a diameter of 29.6 cm (see Fig. 6) connected to a Kontronik PYRO 700–45 Brushless motor. The motor is controlled with an electronic speed control using a Kontronik Jive PRO 80+ HV.

### C. Shielding objects and configuration

Two different shielding geometries were placed between the noise source and the microphone array in the experiments. The first shielding object is a rectangular plate with a dimension of 123 × 24.5 cm. In the follow-up experiments the flat plate is replaced by a NACA 64–008 A wing (see Fig. 7) with the same dimensions as the plate, i.e., a chord of 24.5 cm and a span of 123 cm. The wing is positioned so the upper edge corresponds to the trailing edge and

FIG. 5. (Color online) Customized miniature sound source (omnidirectional in the azimuthal plane).

the bottom edge to the leading edge. The material of both shielding objects is aluminium. Both the flat plate and the wing are fixed using two side plates. Noise diffraction is expected to be more prominent at the longest edges (i.e., the leading and trailing edges), therefore the side plates are not expected to significantly affect the results.

Three parameters are set for the experiments shown in Fig. 8:

- the distance between the source and shielding object, $d_{\text{object}}$,
- the distance between the source and the array, $d_{\text{array}}$,
- the height of the source, $h_{\text{source}}$.

The different experimental setups used in the noise shielding experiments, for the omni-directional source and the propeller are illustrated in Fig. 9. The experiments with the propeller required a support to fix it because it is not possible to suspend it from the ceiling as for the omni-directional source.

FIG. 6. (Color online) Propeller used in the experiments (3-blade Master Airscrew E-MA1260T).

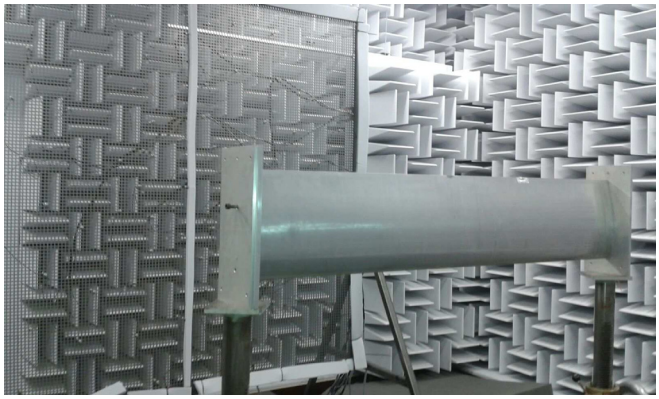

FIG. 7. (Color online) Wing and support used in the experiments.

## IV. RESULTS

### A. Noise shielding of an omni-directional source

This subsection assesses the noise shielding of an omni-directional source by a model wing. First, a flat plate of the same dimensions as the wing is used to compare experimental values of noise shielding with predictions, as it is the simplest case that can be analyzed. The flat plate is then replaced by the wing, and the effect of a smooth edge on the noise shielding is investigated.

The measurements of noise shielding at the microphones are compared with predictions in order to assess the validity of the model. The microphones of the array are also used collectively to perform beamforming. In this way it is possible to visualize the diffraction around the edges of the shielding objects.

Some of the beamforming plots presented in this work show many side lobes. Other beamforming algorithms than the one presented in Sec. II B, such as the CLEAN-SC (Luesutthiviboon *et al.*, 2018), were applied to the experimental data, resulting in plots with less side lobes. However, in this case only one noise source, located at the trailing edge, was detected. The reason is that CLEAN-SC eliminates all sources that are spatially coherent with the main source (Merino-Martinez *et al.*, 2016). Other methods such as CLEAN-PSF or functional beamforming were not applied

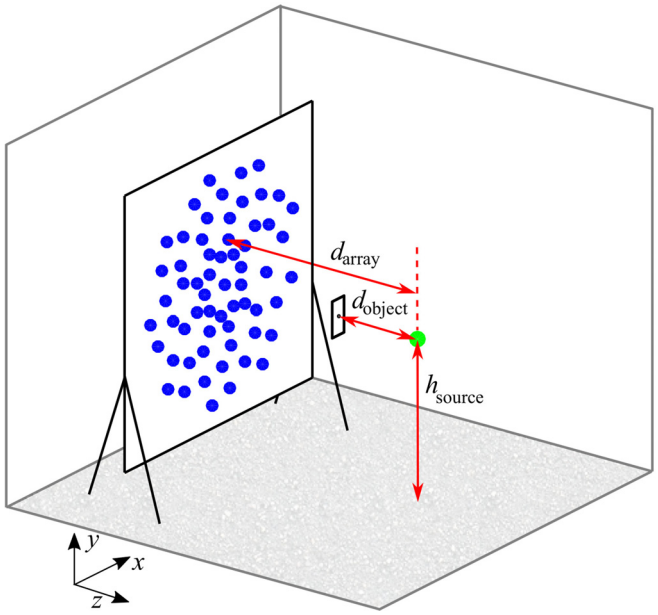


FIG. 8. (Color online) General setup of the experiment in the anechoic room and definition of the distances varied during the experiments.

since the source plots were considered sufficiently clean by applying conventional beamforming.

These beamforming plots of the experimental data are compared with beamforming of the predictions. The beamforming plots of Figs. 10 and 11 correspond to two different cases of noise shielding of the source by the flat plate. These two cases are representative of the lowest (Fig. 10) and highest (Fig. 11) values of $d_{array}$ of the experiments.

The experimental results are in agreement with the predictions for the two cases, with the source of strongest magnitude located at the trailing edge. The experimental results show more side lobes than the beamforming plots obtained from predictions, which are clean around the main source. This behavior is expected as the pressure measured at the microphones can suffer disturbances from the experimental setup used to fix the wing.

The results for the beamformed experimental data also show that the source was not exactly centered at the wing in the $x$ axis, as expected. Therefore beamforming is also a

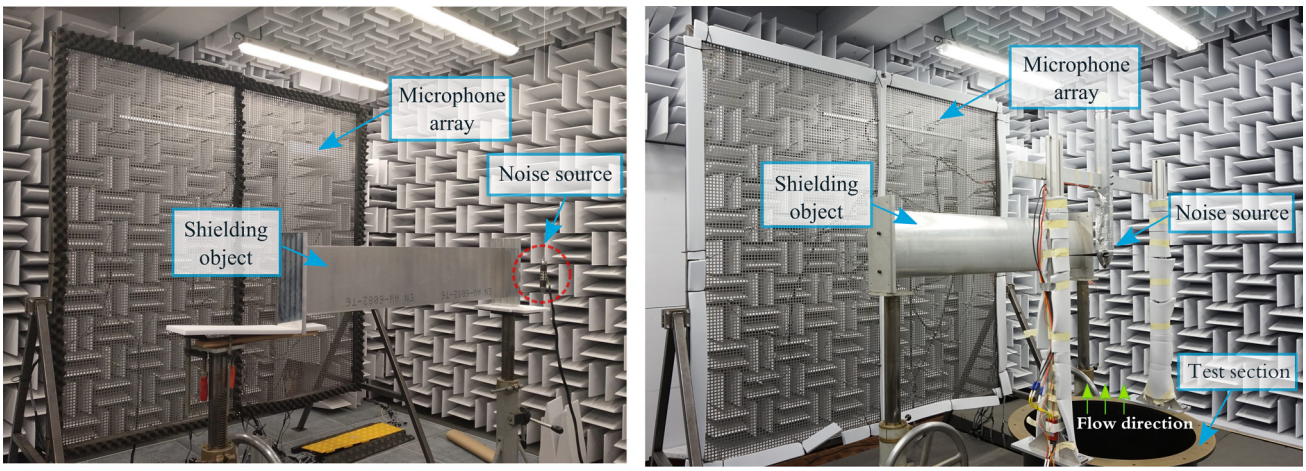


FIG. 9. (Color online) Setup of the experiment in the anechoic room for the omni-directional noise source (left) and the propeller (right).

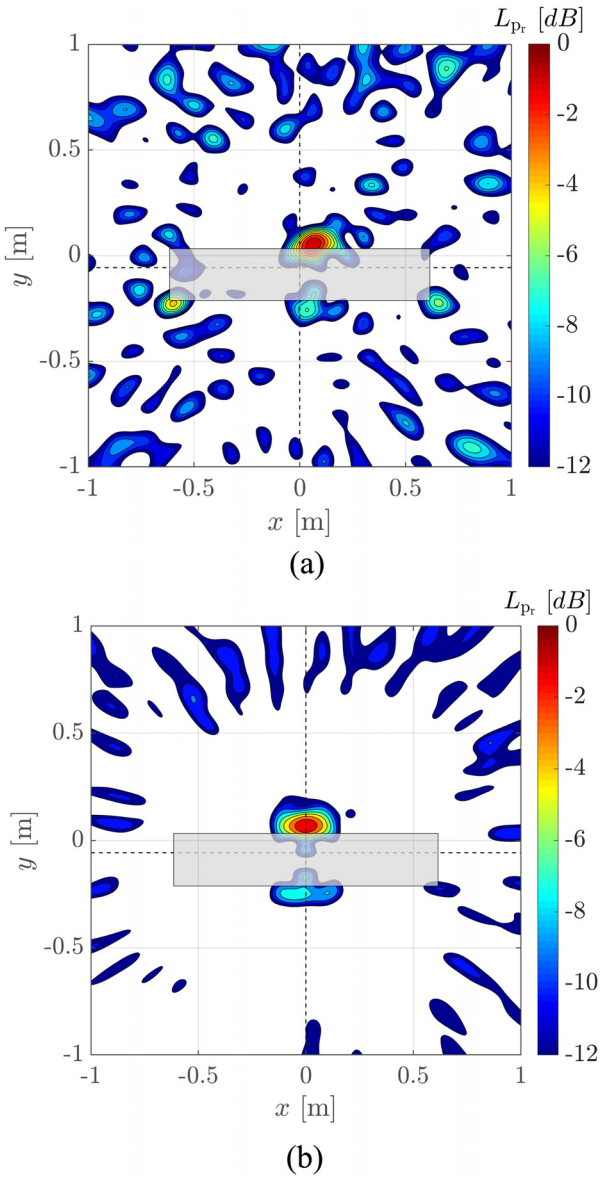


FIG. 10. (Color online) Beamforming plots for the flat plate case and a frequency of 3150 Hz, $d_{\text{array}} = 1.81$ m and $d_{\text{object}} = 0.38$ m: (a) experimental, (b) prediction. The intersection of the dashed lines indicates the source position.

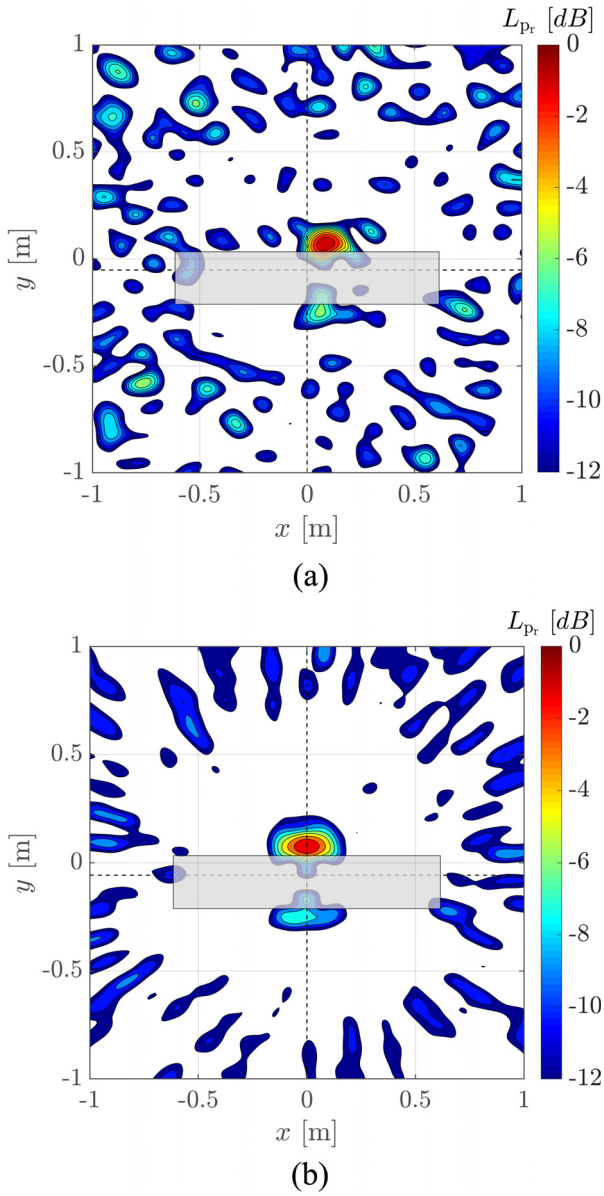


FIG. 11. (Color online) Beamforming plots for the flat plate case and a frequency of 5000 Hz, $d_{\text{array}} = 3.40$ m and $d_{\text{object}} = 0.75$ m: (a) experimental, (b) prediction. The intersection of the dashed lines indicates the source position.

valuable tool to identify the exact position of the noise source and use it as input to obtain more accurate predictions.

This experiment considered six different combinations of $d_{\text{array}}$ and $d_{\text{object}}$, which combined with the 64 microphones in the array results in a large data set of noise shielding values. Therefore, the difference between experimental values of noise shielding and predictions is expressed in terms of an average absolute deviation,

$$\delta = \frac{1}{N}\sum_{n=1}^{N} |\Delta L_{\text{p,prediction}_n} - \Delta L_{\text{p,experimental}_n}|. \tag{20}$$

Here, $N$ is the total number of microphones and $\Delta L_{\text{p,prediction}}$ and $\Delta L_{\text{p,experimental}}$ are the noise shielding values determined in the prediction and experiment, respectively.

The results of $\delta$ for the 1/3-octave bands of 2000, 3150, 4000, and 5000 Hz are presented in Fig. 12. The values of $\delta$ are positioned according to the distance between the source and the array and the source and the shielding object ($d_{\text{array}}$ and $d_{\text{object}}$).

Figure 12 shows that the values of $\delta$ are around 2–3 dB, which confirms the agreement already verified through the beamforming plots of Figs. 10 and 11. The higher values of $\delta$ are observed for the smallest distances $d_{\text{object}}$.

The flat plate was then replaced by the wing, and the noise shielding values are measured for the same distances $d_{\text{array}}$ and $d_{\text{object}}$. Figure 13 presents the new values of $\delta$. Note that the predictions still consider the wing as a sharp-edge object.

The difference between experiments and predictions is noticeably higher now, with Fig. 13 showing values of $\delta$ higher than 5 dB. This indicates that the small curvature of the leading edge affects the results of noise shielding. New

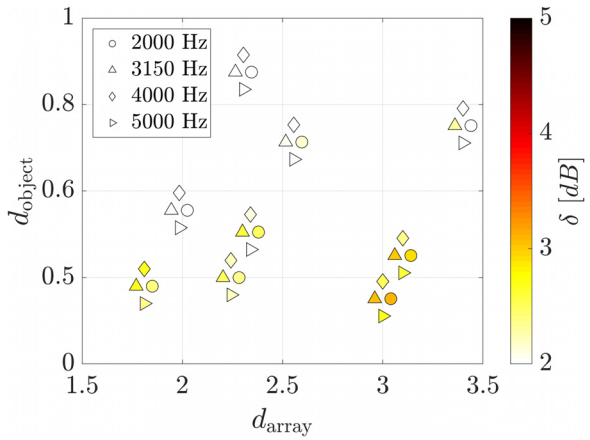


FIG. 12. (Color online) Average absolute deviation in *dB* between experimental results and predictions of noise shielding for the flat plate. The shape of the marker indicates the frequency considered (center frequencies of 1/3-octave bands).

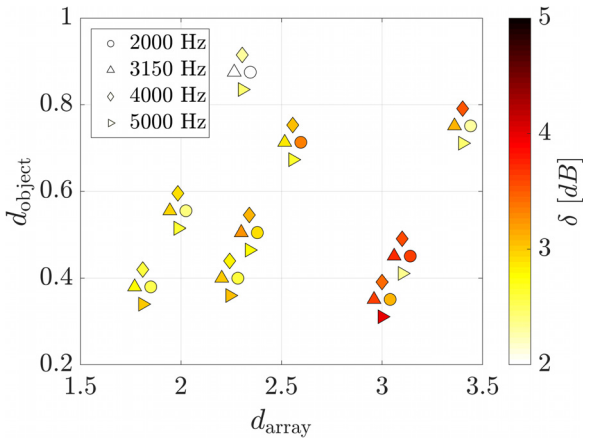


FIG. 14. (Color online) Average absolute deviation in *dB* between experimental results and predictions (considering the curvature of the leading edge) of noise shielding for the wing. The shape of the marker indicates the frequency considered (center frequencies of 1/3-octave bands).

predictions of noise shielding are generated modelling the curvature of the leading edge as half of an ellipse, which results in the values of $\delta$ in Fig. 14.

In Fig. 14 the values of $\delta$ are lower compared to Fig. 13, which shows the importance of accounting for the creeping rays in the predictions. As a next step Fig. 15 presents the beamforming results, in which Fig. 15(a) corresponds to the case of the wing and Fig. 15(b) to the flat plate, for the same values of $d_{\text{array}}$ and $d_{\text{object}}$. The plot for the case of the wing shows sources of the same magnitude at the leading and trailing edge, while in the plot of the flat plate the strongest source is located at the trailing edge, like the cases analyzed before.

Therefore, the smooth leading edge has a significant influence on noise diffraction, a behavior expected specially at high frequencies (Keller, 1961). This is corroborated by the beamforming plot of Fig. 16, which corresponds to the prediction, considering the creeping rays, and shows two equally strong sources at the leading and trailing edge, as in the experimental plot of Fig. 15(a).

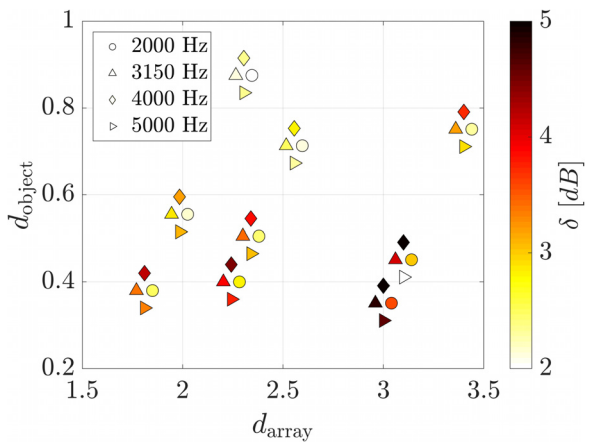


FIG. 13. (Color online) Average absolute deviation in *dB* between experimental results and predictions (without considering the curvature of the leading edge) of noise shielding for the wing. The shape of the marker indicates the frequency considered (center frequencies of 1/3-octave bands).

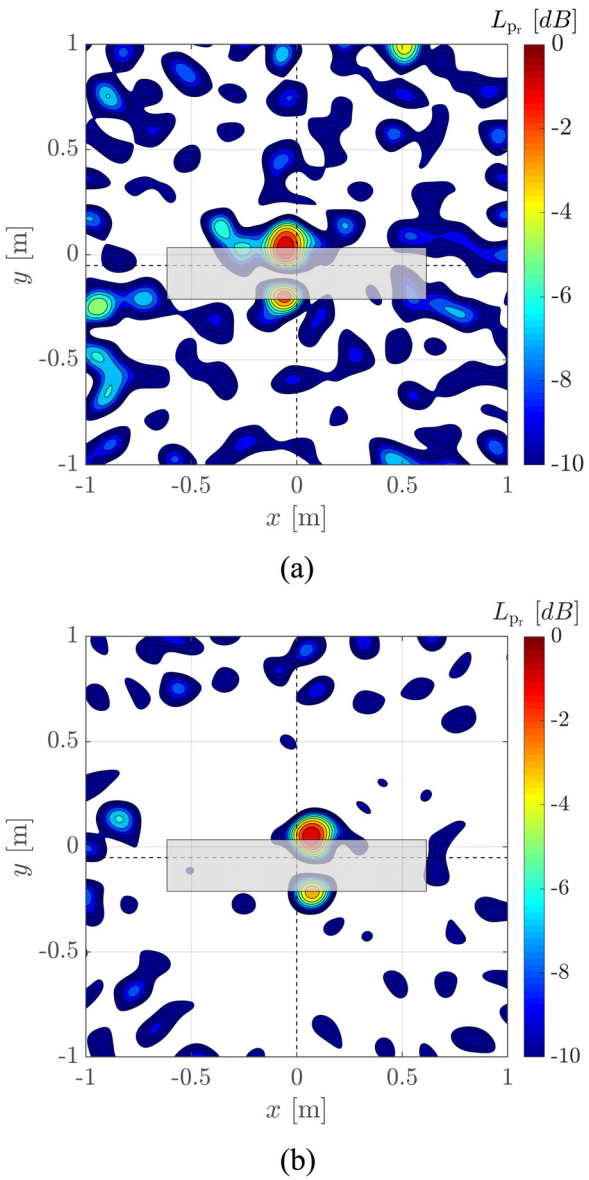


FIG. 15. (Color online) Experimental beamforming plots for a frequency of 4000 Hz, $d_{\text{array}} = 3.1$ m and $d_{\text{object}} = 0.45$ m: (a) for the wing, (b) for the flat plate.

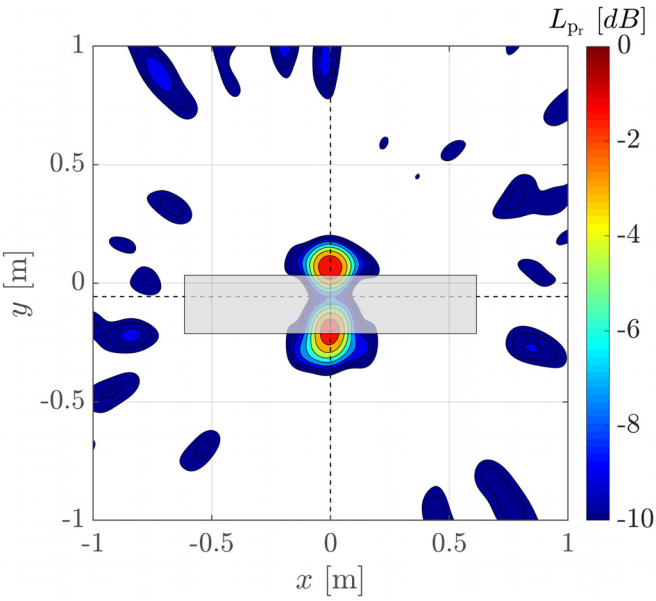


FIG. 16. (Color online) Predicted beamforming plot for a frequency of of 4000 Hz, $d_{array} = 3.1$ m and $d_{object} = 0.45$ m, considering a smooth leading edge.

From these results it can be concluded that noise shielding is very dependent of the shape of the shielding object, such that even for small curvatures the error between experiments and predictions can get significantly increased. It also shows that beamforming is an important tool for the comparison between experiments and predictions to understand the diffraction behaviour at the shielding object.

## B. Noise shielding of a propeller

### 1. Experimental assessment of noise shielding

This section investigates the noise shielding of a small three-blade propeller by the same wing used in Sec. IV A. In this experiment the position of the propeller relative to the array was not varied due to the complex structure required to fix the propeller and minimize the vibrations. Only the wing is moved between the propeller and the microphone array, which limits the number of experiments. Table I shows the relative distances between the wing and the propeller and the array and the propeller. As in Sec. IV A, the distances are defined relative to the noise source. Three different values of rotational speed of the propeller were considered in the experiment.

Extensive research has been done in the field of propeller noise, and even though its directivity is commonly associated with a dipole source (Kurtz and Marte, 1970), propeller noise is composed of thickness noise (monopole), loading noise (dipole), trailing edge noise (quadrupole), and other sources of broadband noise, for example, the shedding of vortices in the flow past a blade.

All these noise sources occur for an ideal isolated propeller. However, in this experiment, other noise sources such as the electrical noise of the propeller and the vibration of the support structure contribute to increasing its complexity. Beamforming is used to understand the behavior of the source, diffraction of noise on the edges of the wing and possible secondary noise sources on the structure.

The experiments were first conducted with no incoming airflow and then under a constant airflow of 10 m/s. A propeller operating with no incoming airflow generates a non-uniform flow, which results in an increase of broadband noise. Still these measurements can be used to assess how much the flow influences noise shielding. In this section, only the results of the propeller under an airflow are analyzed as it is a more realistic situation. For completeness, the results of the propeller under no airflow are presented in the Appendix.

From the experiments it was found that the values of noise shielding are very different for the propeller with and without incoming airflow. Without an incoming airflow there is reinforcement of noise for most frequencies instead of noise shielding. This changes for the propeller with an airflow, which presents significant values of noise shielding. The same behavior was verified for all the values of rotational speed and $d_{object}$ tested.

To illustrate this shielding behavior microphones at the center of the array were selected in the polar and azimuthal directions, as represented in Fig. 17. Figure 18, which illustrates the case for the propeller under an incoming airflow, shows considerable values of noise shielding. The higher

TABLE I. Distances considered in the experiment and values of rotational speed (in RPM) of the propeller.

| | |
|---|---|
| $d_{array}$ [m] | 1.46 |
| $d_{object}$ [m] | 0.40 |
| | 0.54 |
| Rotational speed [rpm] | $RPM_1 = 4400$ |
| | $RPM_2 = 7000$ |
| | $RPM_3 = 7600$ |

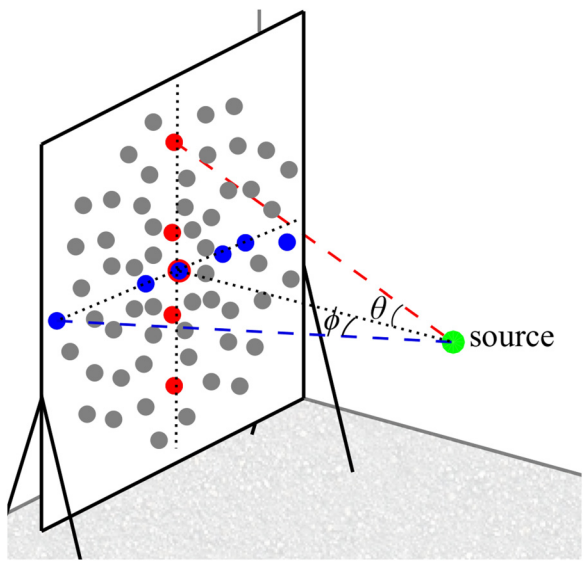


FIG. 17. (Color online) Microphones of the array selected in the azimuthal (blue) and polar (red) directions.

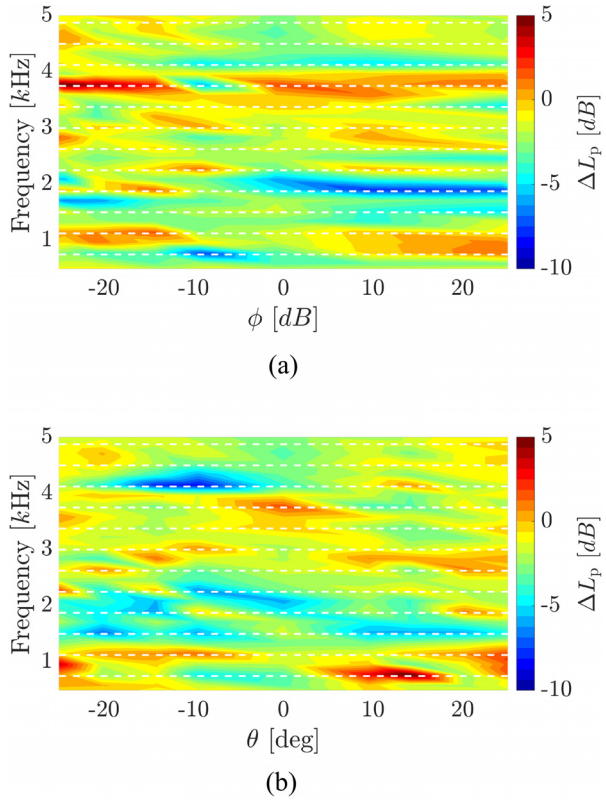


FIG. 18. (Color online) Values of noise shielding as a function of frequency: (a) azimuthal direction, (b) polar direction. The propeller is set at the highest value of rotational speed ($RPM_3$), under a constant airflow of 10 m/s. The white dashed lines correspond to the propeller harmonics.

values of noise shielding are located at the frequencies of the harmonics, represented by dashed white lines.

However, the values of noise shielding for the propeller are less significant than the values measured for the omni-directional source. This can be observed in Fig. 19, which is an equivalent case to Fig. 18 (i.e., with the same relative distances in the experiment) but with the omni-direcional noise source.

Beamforming is used to investigate the reinforcement of noise for the propeller at the frequency of 1300 Hz (see Fig. 18). The result (Fig. 20) shows two sources on the leading and trailing edges of the wing, which indicates noise shielding but also the presence of external noise sources coming from the setup. Other external sources from the support structure, at different frequencies, were found but are not presented in this work. Those sources are likely generated by the interaction of the turbulent flow with the wing and the support structure.

Another case, explored using beamforming, concerns the 7th harmonic (frequency of 2660 Hz), for which there is evidence of noise shielding, according to Fig. 18.

The results are shown in Fig. 21 for the propeller operating at $RPM_3$, and where the distance between the source and the object is the same as in Fig. 20. Figure 21(a) corresponds only to the propeller and Fig. 21(b) to the propeller shielded by the wing. It is seen that the sources move to the edges when the wing is introduced (indicating noise shielding) and there is no presence of external sources.

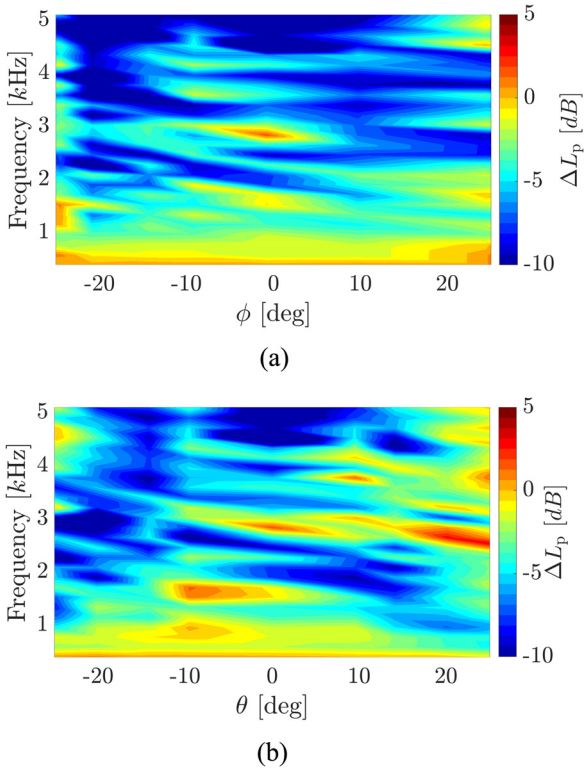


FIG. 19. (Color online) Values of noise shielding as a function of frequency for the omni-directional source: (a) azimuthal direction, (b) polar direction.

This section shows that the propeller is less efficiently shielded by the wing than the omni-directional source and therefore the values of noise shielding depend on the nature of the noise source and consequently of the airflow conditions and interactions with the shielding surface.

### 2. Comparison with predictions considering different types of noise source

Section IV B 1 showed that the values of noise shielding of the propeller differ greatly from the values of noise

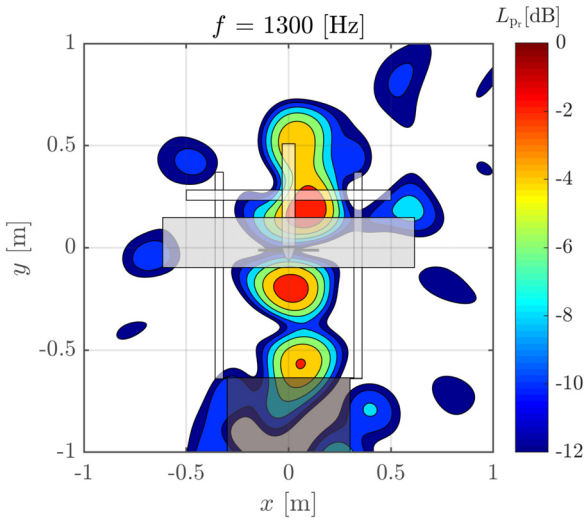


FIG. 20. (Color online) Beamforming plot for a frequency of 1300 Hz, $d_{object} = 0.40$ m. The propeller is set at $RPM_3$ under a constant incoming airflow of 10 m/s.

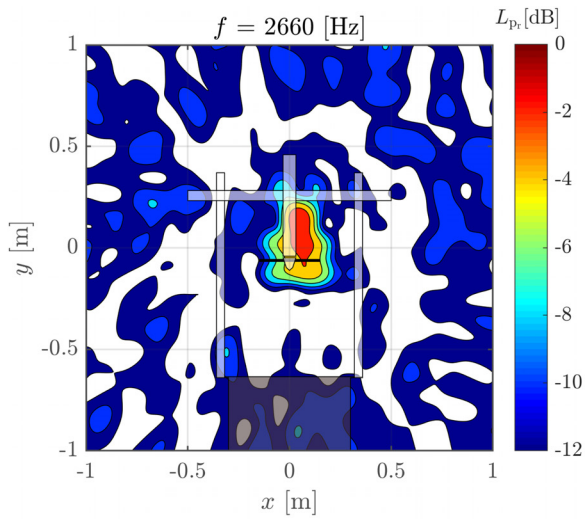


FIG. 21. (Color online) Beamforming plot for a frequency of 2660 Hz, $d_{\text{object}} = 0.40$ m: (a) only the propeller, (b) the propeller and wing. The propeller is set at $\text{RPM}_3$ under a constant incoming airflow of 10 m/s.

shielding of an omni-directional source, i.e., the noise of the propeller is less efficiently shielded by the wing than the noise of the omni-directional source. The approach for predicting noise shielding used in Sec. IV A was found to be appropriate to omni-directional sources, but is not a correct approximation for the propeller.

In this subsection, predictions are compared with the experimental results for the propeller under a constant incoming flow of 10 m/s. Two different types of sources are used in the predictions besides the monopole: a dipole source and a multi-source composed by a ring of monopole sources. All the predictions in this section include the effect of the creeping rays, using the method presented in Sec. II A. The effect of the flow velocity is not accounted for in the noise shielding predictions (such a low velocity is not expected to affect the noise shielding values), however, it is accounted for in the beamforming plots.

As found in Sec. IV B 1, shielding of propeller noise is limited, see as an example Fig. 18, which shows noise shielding less than or equal to 5 dB for most frequencies. For the other two values of rotational speed of the propeller the values of noise shielding were even lower. It was also verified that the higher values of noise shielding are at the frequency of the harmonics. Therefore, for the comparison between experiments and predictions, only the frequencies of the harmonics are selected.

The $L_p$ of the harmonics decreased rapidly after the 5th harmonic and for harmonics higher than the 7th are hardly discernible. In addition, the lowest frequency considered for the analyses corresponds to the 3rd harmonic (roughly 1000 Hz for the three values of angular speed). Low frequencies are not considered because external noise sources are more than or equally significant as the noise of the propeller diffracted by the wing, as found in Sec. IV B 1, and noise shielding does not play an important role. Therefore, only frequencies corresponding to the 3rd to the 7th harmonics are considered for the comparison, which correspond roughly to 1000–3000 Hz.

Different combinations of number of monopoles $N$ and azimuthal number $n$ were tested. It was found that 16 distributed monopoles and a azimuthal number $n = 20$ resulted in a stable solution (i.e., the ring of monopoles resulting in a single compact noise source) for describing a disk shaped source for the range of frequencies considered, and this configuration was used for the predictions with the multi-source.

To better understand the difference in noise shielding between the three types of sources considered in the predictions, the shielding values are plotted as a function of $y$. The propeller is centered at the wing in the $x$ axis. Since the wing covers a big extension of the array in that axis, noise shielding is expected to be approximately constant over $x$ and the values of noise shielding are averaged over $x$ in order to have the variation only dependent of the $y$ axis.

Figure 22 displays the averaged values (over the $x$ axis microphones) of $\Delta L_p$, for the 5th harmonic, when the propeller is set at rotational speed $\text{RPM}_3$, and $d_{\text{object}} = 0.40$ m, observed from the measurements and from model predictions, using as a source a monopole, dipole and multi-source. The value of the prediction using a dipole is not presented at $y = 0$ m because it is a singularity. It can be easily observed that the prediction with the dipole shows better agreement with the experiments.

Another example is represented in Fig. 23, in which the propeller is still set at $\text{RPM}_3$, but $d_{\text{object}} = 0.53$ m and the 4th harmonic is considered. Again, the better agreement is found considering the dipole in the predictions. This is the case for all the harmonics considered, i.e., the ones with values of noise shielding higher than 3 dB for the majority of the microphones and frequencies between 1000 and 3000 Hz.

The monopole seems to be a good approximation for prediction noise shielding at $y = 0$ m, where the dipole is not suitable. The multi-source is a better approximation than the monopole, but still presents a big deviation compared with the experiments. The deviation between

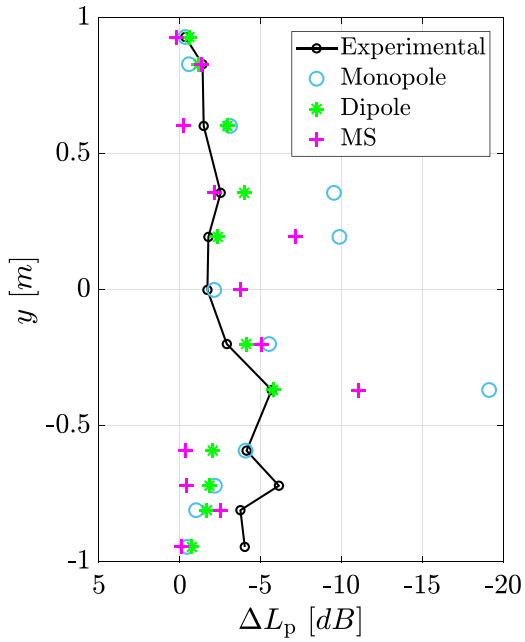


FIG. 22. (Color online) Values of noise shielding along the $y$ axis of the microphone array for the 5th harmonic of the signal. The values are averaged over the $x$ axis. The propeller is set at $RPM_3$ and $d_{object} = 0.40$ m.

experiments and predictions with the monopole and multi-source are specially high for observer positions with higher experimental values of shielding, at $y = \pm 0.2$ m and $y = \pm 0.4$ m, a region where the dipole has the best agreement with the experiments.

## V. CONCLUSION

This work presents an extensive analysis of noise shielding using different types of sources (omni-directional source and a propeller) and shielding objects (flat plate and NACA wing) in a vertical wind tunnel anechoic facility. Experimental data is analyzed and compared with predictions at individual microphone positions and using beamforming to localize the main noise sources.

There is a good agreement between experimental data and predictions when using an omni-directional source in the experiments, both for the plate and the wing as the shielding object (average deviation of 2 to 3 dB).

The good agreement for the case of the wing, however, was only verified when the leading edge was modeled as a smooth edge. This shows that the creeping rays affect the values of noise shielding, even for curvatures with small radius.

The experimental results of noise shielding of the propeller differ greatly from the results obtained for the omni-directional source. Significant values of noise shielding are found when the propeller is under a constant incoming flow. However, such values are low when compared with the omni-directional source. Also, sound at the frequencies of the harmonics is more shielded than broadband noise.

Different types of noise source models were used in the predictions of noise shielding of the propeller: monopole, dipole, and a multi-source composed of monopoles. The dipole showed a good agreement with the experimental data, but both the monopole and the multi-sources greatly overestimated noise shielding.

This work shows that noise shielding is dependent of the directivity of the noise source. An adequate modeling of the source is essential in the predictions, as we observed for the propeller. In addition, the implementation of the monopole and dipole in the shielding tool were validated with experimental data. Beamforming proved to be an important tool in analyzing noise shielding either by showing the diffraction on the edges or by detecting external noise sources.

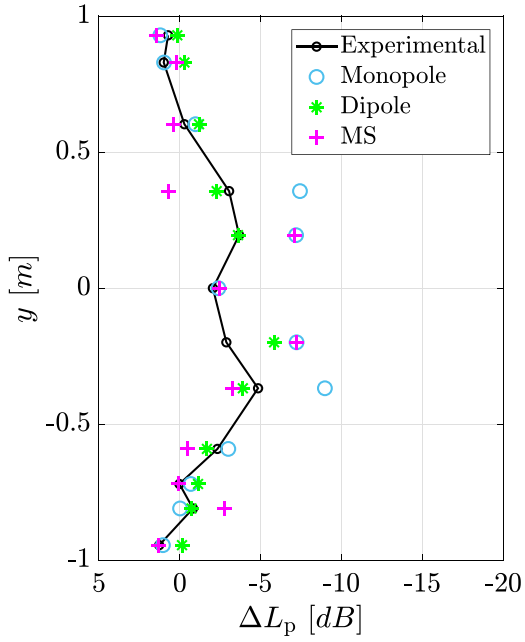


FIG. 23. (Color online) Values of noise shielding along the $y$ axis of the microphone array for the 4th harmonic of the signal. The values are averaged over the $x$ axis. The propeller is set at $RPM_3$ and $d_{object} = 0.53$ m.

## APPENDIX: ANALYSIS OF NOISE SHIELDING OF A PROPELLER WITH NO INCOMING AIRFLOW

The same analysis of Sec. IV B 1 for the propeller under a constant airflow is here repeated for the case of the propeller operating under no airflow.

Consider the azimuthal and polar plots of Fig. 24 for the propeller under no airflow. These plots present higher values of reinforcement of noise, and lower values of noise shielding when compared with the propeller with an inflow of Fig. 18 (note that the scale of Fig. 24 was adjusted to a higher maximum value).

Similarly to what was observed for the propeller with airflow, the frequency of 1300 Hz presents a strong reinforcement of noise. The beamforming plot of Fig. 25 shows a strong source at the top of the tube that supports the electric motor. This source overshadows any noise diffraction.

Now consider the 7th harmonic (frequency of 2660 Hz), also presented in Sec. IV B 1. for the propeller with aiflow. At this frequency there is evidence of noise shielding both

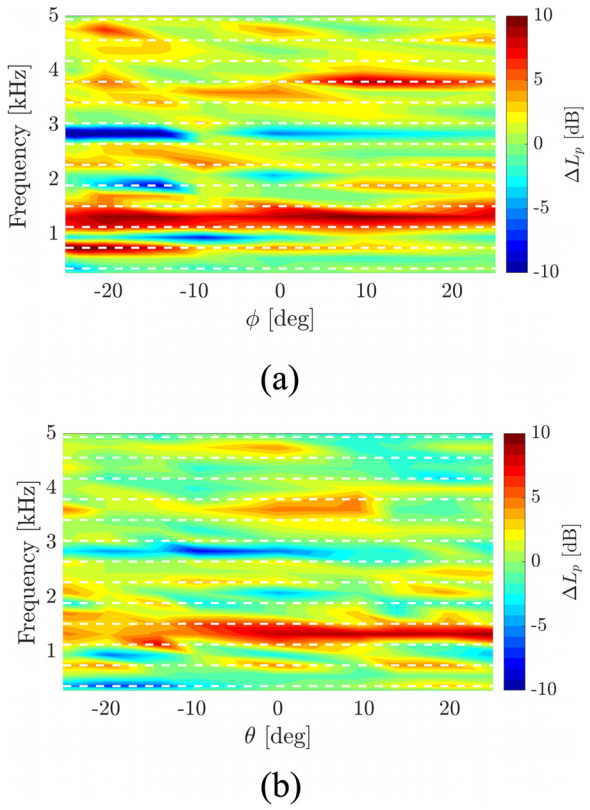


FIG. 24. (Color online) Values of noise shielding as a function of frequency: (a) azimuthal direction, (b) polar direction. The propeller is set at the highest value of rotational speed ($RPM_3$), with no incoming airflow. The white dashed lines correspond to the propeller harmonics.

with and without incoming airflow, according to Figs. 18 and 24.

There are clear differences between Fig. 21(a) and Fig. 26(a). With the propeller under an incoming airflow there is just one source at the top of the propeller disk, while without airflow there are two significant sources (at the top and bottom of the propeller disk). When the wing is introduced, in

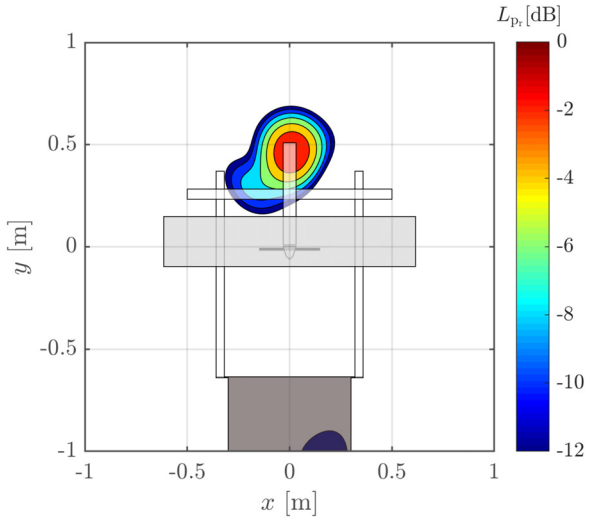


FIG. 25. (Color online) Beamforming plot for a frequency of 1300 Hz, $d_{object} = 0.40$ m. The propeller is set at $RPM_3$ with no incoming airflow.

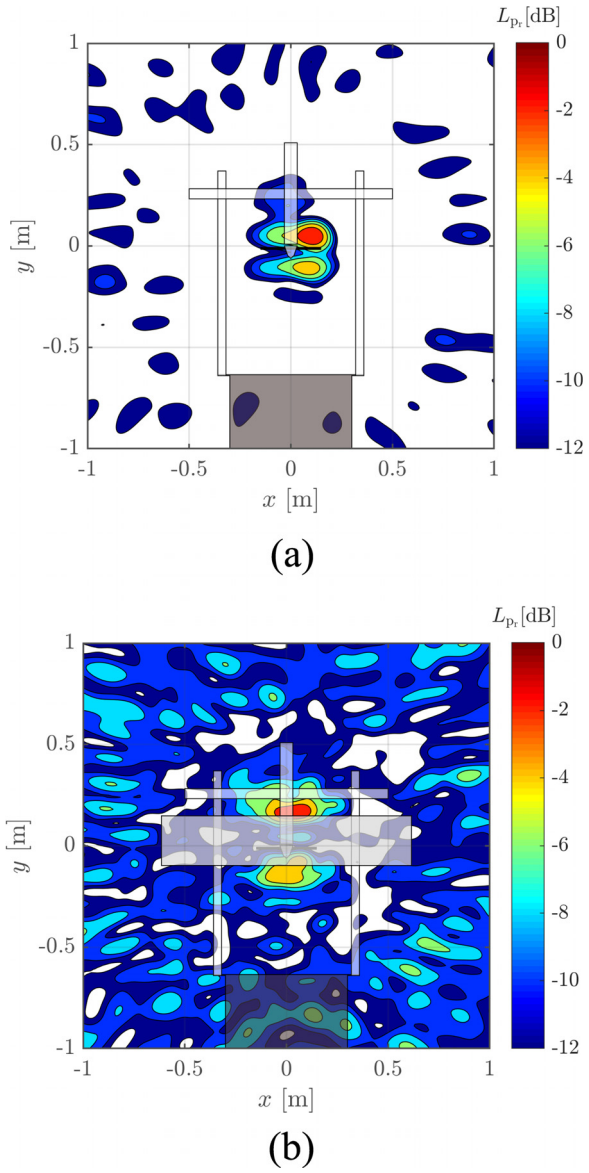


FIG. 26. (Color online) Beamforming plot for a frequency of 2660 Hz, $d_{object} = 0.40$ m: (a) only the propeller, (b) propeller and wing. The propeller is set at $RPM_3$ with no incoming airflow.

Fig. 21(b), the source is diffracted on the edges, similarly to Fig. 26(b), as expected since both cases present noise shielding.


Agarwal, A., Dowling, A. P., Shin, H.-C., Graham, W., and Sefi, S. (**2007**). "Ray tracing approach to calculate acoustic shielding by a flying wing airframe," AIAA J. **45**(5), 1080–1090.

Born, M., and Wolf, E. (**1999**). *Principles of Optics, Electromagnetic Theory of Propagation, Interference and Diffraction of Light* (Cambridge University Press, Cambridge).

Colas, D., and Spakovszky, Z. (**2013**). "A turbomachinery noise shielding framework based on the modified theory of physical optics," in *19th AIAA/CEAS Aeroacoustics Conference*, Berlin, Germany, AIAA Paper 2013-2136.

Dunn, M., and Tinetti, A. (**2004**). *Aeroacoustic Scattering via the Equivalent Source Method* (American Institute of Aeronautics and Astronautics, Reston, VA).

Guo, Y., Czech, M., and Thomas, R. H. (**2015**). *Open Rotor Noise Shielding by Blended-Wing-Body Aircraft* (American Institute of Aeronautics and Astronautics, Reston, VA).

ISO (**2012a**). 3745, *Acoustics—Determination of Sound Power Levels and Sound Energy Levels of Noise Sources Using Sound Pressure—Precision*

*Methods for Anechoic Rooms and Hemi-Anechoic Rooms*, Tech. Rep. 3 (International Organization for Standardization, Geneva).
ISO (**2012b**). 3382, *Acoustics—Measurements of Room Acoustics Parameters* (International Organization for Standardization, Geneva).
Keller, J. (**1961**). "Geometrical theory of diffraction," J. Opt. Soc. Am. **52**(2), 116–130.
Kirkup, S. (**2007**). *The Boundary Element Method in Acoustics* (Integrated Sound Software, Todmorden, UK), Chap. 1.
Kurtz, D. W., and Marte, J. E. (**1970**). "A review of aerodynamic noise from propellers, rotors, and lift fans," National Aeronautics and Space Administration, Technical Report No. 32-1462.
Leppington, F. (**1970**). "Curvature effects in the diffraction of short waves into a shadow," Aeronautical Research Council.
Lewist, R., and Boersma, J. (**1969**). "Uniform asymptotic theory of edge diffraction," J. Math. Phys. **10**(12), 2291–2305.
Lu, C., and Morrell, P. (**2006**). "Determination and applications of environmental costs at different sized airports—Aircraft noise and engine emissions," Transportation **33**, 45–61.
Luesutthiviboon, S., Malgoezar, A., Snellen, M., and Simons, D. (**2018**). "Maximizing source discrimination performance by using an optimized array and adaptive high-resolution clean-sc beamforming," in *Berlin Beamforming Conference 2018*.
Maekawa, Z. (**1968**). "Noise reduction by screens," Appl. Acoust. **1**(3), 157–173.
Malgoezar, A., Snellen, M., Sijtsma, P., and Simons, D. (**2016**). "Improving beamforming by optimization of acoustic array microphone positions," in *6th Berlin Beamforming Conference, BeBeC-2016-S5*.
Manoha, E., Redonnet, S., and Caro, S. (**2010**). "Computational Aeroacoustics," in *Encyclopedia of Aerospace Engineering*, edited by R. Blockley and W. Shyy (Wiley, Chichester, UK).
Merino-Martinez, R., Snellen, M., and Simons, D. G. (**2016**). "Functional beamforming applied to imaging of flyover noise on landing aircraft," J. Aircr. **53**(6), 1830–1843.
Miyamoto, K., and Wolf, E. (**1962**). "Generalization of the Maggi-Rubinowicz theory of the boundary diffraction wave—Part I," J. Opt. Soc. Am. **6**(6), 615–625.
Oppenheim, A. V., Willsky, A., and Nawab, S. (**1997**). *Signals and Systems*, 2nd ed. (Pearson, Harlow, UK).
Pathak, P., Burnside, W., and Marhefka, R. (**1979**). "A uniform GTD analysis of the scattering of electromagnetic waves by a smooth convex surface" Electroscience Laboratory, Ohio State University, Technical Report No. 784583-4.
Sarradj, E. (**2012**). "Three-dimensional acoustic source mapping with different beamforming steering vector formulations," Adv. Acoust. Vib. **2012**, 292695.
Sommerfeld, A. (**2004**). *Mathematical Theory of Diffraction* (Springer, Berlin).
Synodinos, A., Self, R., and Torija, A. (**2017**). "Noise assessment of aircraft with distributed electric propulsion using a new noise estimation framework," in *24th International Congress on Sound and Vibration*, London, UK (23–27 July).
Turkdogru, N., Ahuja, K. K., and Gaeta, R. J. (**2013**). "Validity of the point source assumption of a rotor for farfield acoustic measurements with shielding," Int. J. Aeroacoust. **12**(4), 363–385.
Umul, Y. (**2004**). "Modified theory of physical optics," Opt. Express **12**(20), 4959–4972.
Vieira, A., Snellen, M., and Simons, D. G. (**2018**). "Assessing the shielding of engine noise by the wings for current aircraft using model predictions and measurements," J. Acoust. Soc. Am. **143**(1), 388–398.
Vlemmix, C. (**2017**). "Acoustic array design: The design of a reconfigurable phased microphone array for aeroacoustic wind tunnel measurements," MSc. thesis, Delft University of Technology, Delft, the Netherlands.